

MATTERS ARISING

Is *p*-type doping in TeO₂ feasible?

Zewen Xiao,^{1,*} Chen Qiu,² Su-Huai Wei,² and Hideo Hosono³

¹Wuhan National Laboratory for Optoelectronic, Huazhong University of Science and Technology, Wuhan 430074, China

²Eastern Institute of Technology, Ningbo 315200, China

³MDX Research Center for Element Strategy, International Research Frontiers Initiative, Tokyo Institute of Technology, Yokohama 226-8501, Japan

Email: zwxiao@hust.edu.cn

ARISING FROM A. Zavabeti et al. *Nature Electronics* <https://doi.org/10.1038/s41928-021-00561-5> (2021)

High-performance transparent oxide semiconductors (TOSs) are crucial for the advancement of next-generation transparent electronics, power electronics and energy-efficient displays. The lack of high-mobility, *p*-type TOSs presents a significant challenge in designing bipolar transistors, inverter circuits, and transparent thin-film transistors (TFTs). This challenge arises from the deep and localized valence band maxima (VBMs) primarily composed of O 2p orbitals, hindering the generation and transport of holes.¹ To address this issue, a common strategy involves elevating and dispersing the VBM by utilizing cations with high-lying occupied d^{10} or s^2 orbitals that can effectively hybridize with O 2p orbitals.² Notably, the use of Cu(I) with the highest-lying d^{10} orbitals has facilitated the realization of Cu(I)-based *p*-type TOSs, exemplified by CuAlO₂.^{2,3} On the other hand, cations with s^2 states conform to a specific atomic energy level sequence: Sn(II) → Pb(II) → Sb(III) → Bi(III) → Te(IV) → Po(IV).⁴ For instance, SnO is recognized as a *p*-type semiconductor with a high-lying *s*-like VBM at −5.8 eV relative to the vacuum level.⁵ In contrast, PbO encounters challenges in hole doping due to its deeper $6s^2$ states induced by relativistic effects,⁴ resulting in a VBM at −6.2 eV.⁶ Following this trend, it is anticipated that Sb₂O₃, Bi₂O₃, TeO₂, and PoO₂ may encounter similar obstacles in serving as *p*-type TOSs.

Interestingly, in their Article, Zavabeti et al.⁷ presented a remarkable finding showcasing two-dimensional (2D) β -TeO₂ as a high-mobility *p*-type TOS with a 2D hole density (p_{2D}) of $1.04 \times 10^9 \text{ cm}^{-2}$ and an impressive hole mobility of $141 \text{ cm}^2 \text{ V}^{-1} \text{ s}^{-1}$. This discovery challenges the conventional perception of TeO₂ as an insulator⁸ and contradicts the anticipated difficulty in hole doping according to established trends. Notably, Zavabeti et al.⁷ observed that the Fermi level (E_F) of 2D β -TeO₂ is situated approximately 0.9 eV above the VBM (refer to [Fig. 3b in Ref. 7](#)). Calculation using the formula $p_{2D} = N_{v,2D} \exp[-(E_F - E_v)/k_B T]$ (where $N_{v,2D}$ represents the effective density of states in the valence band, typically around 10^{12} cm^{-2} , k_B is the Boltzmann constant, and T is the absolute temperature) suggests that with the reported E_F , the p_{2D} value at room temperature is negligible, less than 1 cm^{-2} (essentially zero). This implies insulating properties for 2D β -TeO₂, which sharply contrasts with the documented *p*-type conductivity demonstrating a p_{2D} value of $1.04 \times 10^9 \text{ cm}^{-2}$.

Zavabeti et al. synthesized the 2D β -TeO₂ by high-temperature surface oxidation of a eutectic mixture containing Te (5 wt%) and Se (95 wt%). Despite their efforts, residual Se was

identified in the 2D β -TeO₂ samples due to Se's lower oxophilicity relative to Te (refer to [Extended Fig. 3 in Ref. 7](#)). Furthermore, the potential reduction of an extremely thin layer of β -TeO₂ to elemental Te remains a plausible event. TeO₂ is known to undergo partial decomposition either spontaneously or upon heating, resulting the generation of tellurium suboxide (TeO_{2-x}, where x typically ranges from 0.7 to 0.9) and elemental Te.⁹ Moreover, when subjected to an applied voltage of several volts, the intense electric field strength across the ultrathin layer can easily surpass the breakdown voltage, leading to the formation of elemental Te. Notably, elemental Se, elemental Te, and Te_{1-x}Se_x alloy are all well-known high-mobility p -type semiconductors with three-dimensional (3D) hole densities (p_{3D}) on the order of 10^{14} cm⁻³ (equivalent to p_{2D} on the order of 10^9 cm⁻²) and high hole mobilities ranging from hundreds to over a thousand cm² V⁻¹ s⁻¹,¹⁰⁻¹² comparable to those observed in the 2D β -TeO₂ samples. Thus, it is crucial to elucidate the true source of the p -type conductivity in the 2D β -TeO₂ samples, whether originating from the 2D β -TeO₂ itself, residual elemental Se, reduced elemental or even Te_{1-x}Se_x, warranting further investigation.

The discussion now shifts towards assessing the dopability of TeO₂ to enhance our comprehension of its electrical properties. The dopability of a semiconductor can be effectively evaluated from its band edge positions.¹³ Generally, a semiconductor is more readily doped with electrons when its conduction band minimum (CBM) is deeper, and with holes when its VBM is shallower. Semiconductors prone to electron doping (e.g., ZnO, In₂O₃, and SnO₂) typically have a CBM deeper than approximately -4.0 eV, while semiconductors amenable to hole doping (e.g., SnO, NiO, and CuAlO₂) generally exhibit a VBM shallower than about -6.0 eV.² These empirical benchmarks have steered the investigation of transparent semiconductors, particularly those of the p -type variety. For instance, contrary to expectations, PbO, a p -type SnO homolog, encountered impediments in hole doping due to its VBM (-6.2 eV), surpassing the empirical VBM threshold.⁶ Concerning TeO₂, which manifests in three polymorphs (α -, β -, and γ -TeO₂) as illustrated in [Supplementary Fig. 1](#), first-principles calculations (refer to [computational methods in Supplementary Information](#)) unveil that the CBMs are shallower than the empirical CBM threshold of -4.0 eV, while the VBMs are deeper than the empirical VBM threshold of -6.0 eV, as depicted in [Fig. 1](#). This signals challenges in carrier doping for α -, β -, and γ -TeO₂, aligning with their recognized insulating traits. In contrast to 3D β -TeO₂, the 2D β -

TeO₂ monolayer displays a deeper VBM and a shallower CBM, posing increased hurdles in carrier doping. The deep VBM and the ensuing difficulty in achieving *p*-type doping in TeO₂ can be attributed to the relatively deep Te 5s² orbital (Supplementary Table 2), which exhibits insufficient hybridization with O 2p orbitals (Supplementary Fig. 2) and therefore cannot elevate the VBM as effectively as the high-lying Cu 3d¹⁰ and Sn 5s² orbitals.

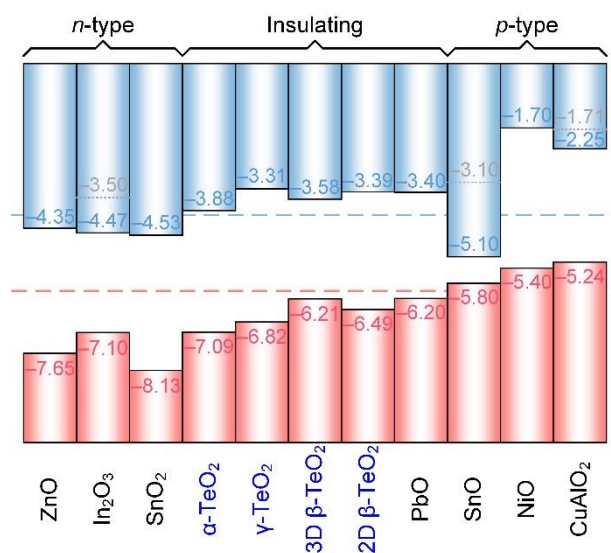


Fig. 1 | Band alignment of TeO₂ polymorphs and related oxides. The energies are with respect to the E_{vac} . The data for the TeO₂ polymorphs is theoretical, while the data for other compounds is experimental (Supplementary Table 1). Empirically, semiconductors with CBM deeper than the blue dashed line (-4 eV) can be doped *n*-type, while semiconductors with VBM shallower than the red dashed line (-6 eV) can be doped *p*-type.

The dopability of TeO₂ can also be elucidated by examining the thermodynamics of its intrinsic defects. Fig. 2 presents the calculated defect formation energies of both 3D and 2D β-TeO₂. Notably, all intrinsic defects exhibit relatively high formation energies, approaching or exceeding 1 eV at equilibrium, with deep transition levels (also depicted in Supplementary Fig. 3), signifying the absence of effective donors and acceptors. For 3D β-TeO₂ synthesized at room temperature, the calculated equilibrium E_F ($E_{F,e}$) is situated at mid-gap (consistent across chemical conditions, as displayed in Fig. 2a and 2b), correlating with zero carrier density (refer to Supplementary Table 3). Elevating the growth temperature (T_G) to a sufficiently high temperature of 700 K marginally shift the $E_{F,e}$ away from mid-gap; however, the carrier densities (electron density n_0 of 8.2×10^5 cm⁻³ under the Te-rich condition, $p_0 = 3.1 \times 10^{10}$ cm⁻³

under the O-rich condition) remain insufficient for typical semiconductor behavior. In the case of 2D β -TeO₂, the calculated $E_{F,e}$ consistently resides at mid-gap, irrespective of chemical conditions and T_G , as demonstrated in Fig. 2c and 2d. Moreover, donors and acceptors will spontaneously form in the p -type and n -type E_F regions, respectively, owing to their negative formation energies, rendering external doping ineffective in altering its insulating traits.

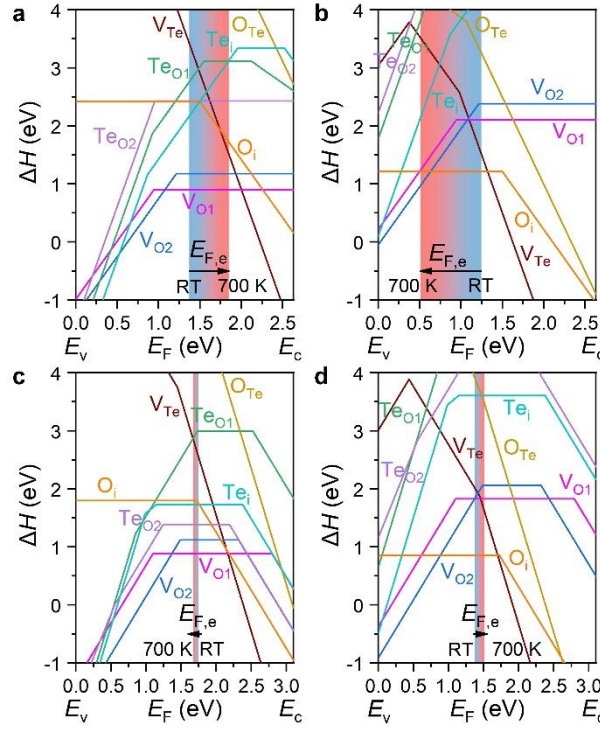


Fig. 2 | Defect formation energies and equilibrium E_F . Calculated formation energies (ΔH) of intrinsic defects as a function of the Fermi level (E_F) for 3D β -TeO₂ (a,b) and 2D β -TeO₂ (c,d) under Te-rich (a,c) and O-rich (b,d) conditions. The colored bars represent the ranges of equilibrium E_F ($E_{F,e}$) solved with growth temperatures ranging from room temperature to a sufficient high temperature of 700 K.

In summary, our investigation unveils that TeO₂, whether in 3D bulk forms (α -, β -, or γ -TeO₂) or in 2D β -TeO₂ layers, encounters substantial obstacles in electrons and hole doping due to its excessively shallow CBM and excessively deep VBM, respectively, causing it to inherently exhibit insulating characteristics. Consequently, the observed p -type conductivity in the 2D β -TeO₂ samples by Zavabeti et al. likely stems from residual elemental Se, reduced elemental Te, or even Te_{1-x}Se_x alloy, all of which function as high-mobility p -type semiconductors.

References

1. Cai, X. & Wei, S.-H. Perspective on the band structure engineering and doping control of transparent conducting materials. *Appl. Phys. Lett.* **119**, (2021).
2. Hosono, H. Exploring Electro-active Functionality of Transparent Oxide Materials. *Jpn. J. Appl. Phys.* **52**, 090001 (2013).
3. Kawazoe, H. *et al.* P-type electrical conduction in transparent thin films of CuAlO₂. *Nature* **389**, 939–942 (1997).
4. Walsh, A., Payne, D. J., Egdell, R. G. & Watson, G. W. Stereochemistry of post-transition metal oxides: revision of the classical lone pair model. *Chem. Soc. Rev.* **40**, 4455–63 (2011).
5. Nomura, K., Kamiya, T. & Hosono, H. Ambipolar Oxide Thin-Film Transistor. *Adv. Mater.* **23**, 3431–3434 (2011).
6. Liao, M. *et al.* Difficulty of carrier generation in orthorhombic PbO. *J. Appl. Phys.* **119**, 165701 (2016).
7. Zavabeti, A. *et al.* High-mobility p-type semiconducting two-dimensional β -TeO₂. *Nat. Electron.* **4**, 277–283 (2021).
8. Keerthana & Venimadhav, A. TeO₂: A Prospective High-k Dielectric. *Phys. status solidi – Rapid Res. Lett.* **18**, 2–8 (2024).
9. Hodgson, S. N. B. & Weng, L. Chemical and sol–gel processing of tellurite glasses for optoelectronics. *J. Mater. Sci. Mater. Electron.* **17**, 723–733 (2006).
10. Heleskivi, J., Stubb, T. & Suntola, T. Direct-Current Measurement of the Hall Effect in Trigonal Selenium Single Crystal. *J. Appl. Phys.* **40**, 2923–2927 (1969).
11. Beyer, W., Mell, H. & Stuke, J. Conductivity and thermoelectric power of trigonal Se_xTe_{1-x} single crystals. *Phys. Status Solidi* **45**, 153–162 (1971).
12. Champness, C. H. & Kipling, A. L. Transport measurements in annealed single crystal tellurium. *Can. J. Phys.* **48**, 3038–3046 (1970).
13. Zhang, S. B., Wei, S.-H. & Zunger, A. A phenomenological model for systematization and prediction of doping limits in II–VI and I–III–VI₂ compounds. *J. Appl. Phys.* **83**, 3192–3196 (1998).

Acknowledgements

This work was supported by the National Natural Science Foundation of China (grants no. 52372150, 12088101, and 11991060) and the National Key R&D Program of China (2022YFB4200305).

Author contributions

Z.X. conceptualized the idea and performed the calculations. Z.X., C.Q., S.-H.W., and H.H. interpreted the results and wrote the paper.

Competing interests

The authors declares no competing interests.

Supplementary Information for:

MATTERS ARISING

Is *p*-type doping in TeO₂ feasible?

Zewen Xiao,^{1,*} Chen Qiu,² Su-Huai Wei,² and Hideo Hosono³

¹Wuhan National Laboratory for Optoelectronic, Huazhong University of Science and Technology, Wuhan 430074, China

²Eastern Institute of Technology, Ningbo 315200, China

³MDX Research Center for Element Strategy, International Research Frontiers Initiative, Tokyo Institute of Technology, Yokohama 226-8501, Japan

Email: zwxiao@hust.edu.cn

ARISING FROM A. Zavabeti et al. *Nature Electronics* <https://doi.org/10.1038/s41928-021-00561-5> (2021)

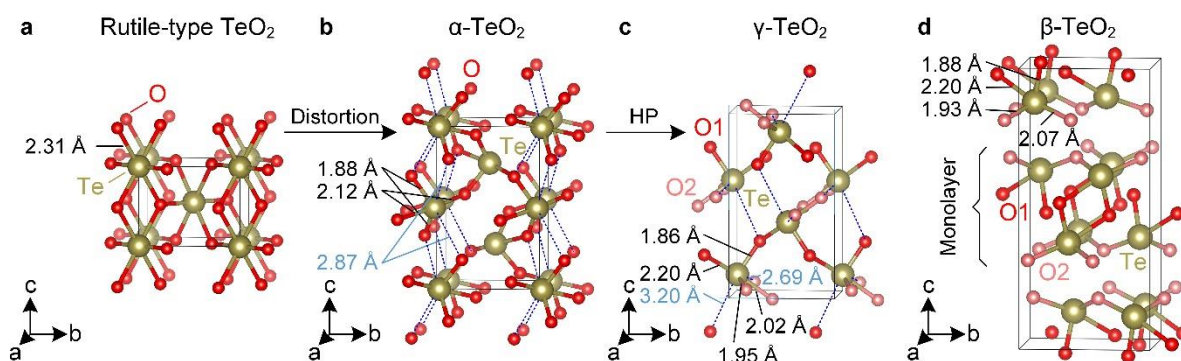
Contents:

Supplementary Fig. 1–3

Supplementary Table 1-3

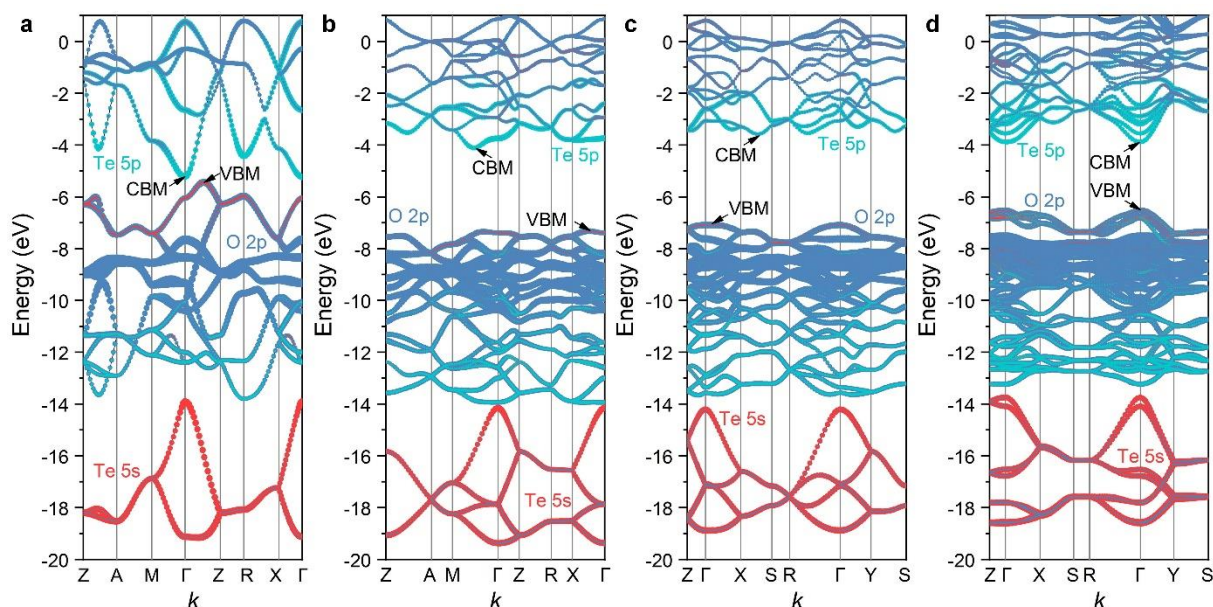
Computational methods

Supplementary references



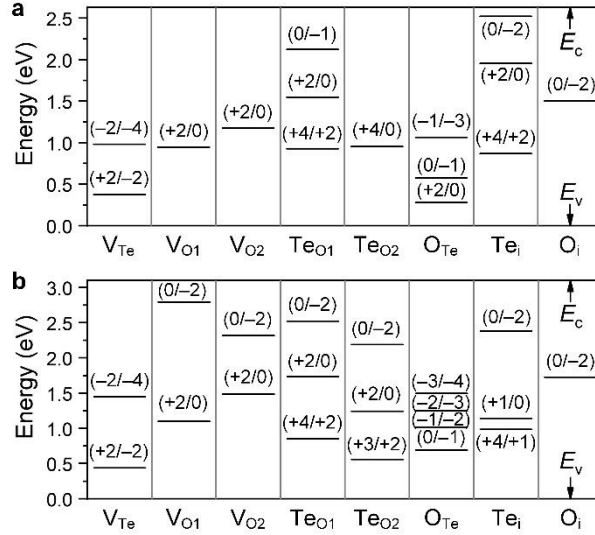
Supplementary Fig. 1 | Crystal of TeO₂ polymorphs: a, hypothetical rutile-type TeO₂ (space group $P4_2/mnm$), **b**, paratellurite α -TeO₂ (space group $P4_12_12$), **c**, γ -TeO₂ (space group $P2_12_12_1$) and **d**, tellurite β -TeO₂ (space group $Pbca$).

The synthetic, colorless tetragonal α -TeO₂ (paratellurite) under ambient conditions was previously reported to exhibit a high-symmetry rutile-type structure (space group $P4_2/mnm$),¹ where each Te atom is coordinated by six O atoms, with a Te—O bond length of 2.30 Å, as shown in [supplementary Fig. 1a](#). Subsequent studies¹ revised the structure of α -TeO₂ to a distorted rutile-type with space group $P4_12_12$ and a doubled c axis, as depicted in [supplementary Fig. 1b](#). Despite this distortion, each Te atom remains 6-coordinated, forming a highly distorted octahedron, where the two short “quasi-equatorial” bonds, two short non-equatorial bonds, and two long non-equatorial bonds are 2.12 Å, 1.88 Å, and 2.87 Å, respectively. More often than not, the two long bonds are excluded, and Te is considered 4-coordinated. Thus, α -TeO₂ can be described as a three-dimensional network of corner-sharing TeO₄ or TeO₄ E (E represents the lone pair of Te) disphenoids. At high pressures above 0.91 GPa,² α -TeO₂ transforms into a lower-symmetry phase (referred to as γ -TeO₂), which belongs to the orthorhombic space group $P2_12_12_1$, as illustrated in [supplementary Fig. 1c](#). This phase transition involves the splitting of the tetragonal a lattice parameter into the unequal a and b orthorhombic parameters, causing the splitting of O sites (denoted as O1 and O2) and resulting in varied bond lengths. The four shorter Te—O bond lengths range from 1.86 to 2.20 Å, while the two longer Te—O bond lengths are 2.69 Å and 3.20 Å, respectively. On the other hand, as illustrated in [supplementary Fig. 1d](#), the naturally occurring yellow mineral tellurite (β -TeO₂) crystallizes in an orthorhombic layered structure,^{3,4} which crystallographically resembles brookite, the orthorhombic variant of TiO₂. Unlike the three-dimensional networks of α -TeO₂ and γ -TeO₂, in which the TeO₄ disphenoids are corner-sharing, the two-dimensional layers in β -TeO₂ consist of TeO₄ disphenoids by sharing alternately the O corners and the O—O edges. Each layer contains two types of O positions in: those inside the layer (labeled O1) and those on the layer’s surface (labeled O2). When β -TeO₂ consists of only one or a few layers, the so-called 2D β -TeO₂ is obtained.^{5,6}



Supplementary Fig. 2 | Calculated band structures of TeO₂ polymorphs: **a**, hypothetical rutile-type TeO₂ (space group $P4_2/mnm$), **b**, paratellurite α -TeO₂ (space group $P4_12_12$), **c**, γ -TeO₂ (space group $P2_12_12_1$) and **d**, tellurite β -TeO₂ (space group $Pbca$). The energies are with respect the vacuum level (zero energy).

For the hypothetical rutile-type TiO₂, the calculated band structure is shown in [Supplementary Fig. 2a](#). The structure reveals an indirect bandgap of only 0.20 eV, which may explain the metallic behavior of recently-reported r-TiO₂ thin films on the FeTe surface.⁷ The VBM consists of antibonding states of O 2p and Te 5s orbitals, while CBM is predominantly derived from Te 5p orbitals. Despite the substantial energy difference between Te 5s and O 2p orbitals (−15.1 eV vs. −9.0 eV, see [Supplementary Table 3](#)), the high symmetry of r-TiO₂ results in a significant coupling between these orbitals, resulting in a notably elevated VBM. Moreover, the high symmetry permits excellent dispersion of the conduction band derived from Te 5p orbitals. As r-TeO₂ distorts into α -TeO₂, shown in [Supplementary Fig. 2b](#), the coupling between Te 5s and O 2p orbitals weakens dramatically, leading the VBM to be primarily composed of O 2p orbitals with minor contribution from the Te 5s states. The structural distortion also narrows the conduction band derived from Te 5p orbitals, widening the calculated bandgap of α -TeO₂ to 3.21 eV, which align with optical transparency. For the high-pressure orthorhombic γ -TeO₂ ([Supplementary Fig. 2c](#)), its band structure is similar to that of tetragonal α -TeO₂, but with a slightly larger bandgap, likely attributed to further symmetry reduction and bond breaking from α - to γ -TeO₂. In contrast, β -TeO₂ ([Supplementary Fig. 2d](#)) exhibits a markedly different band structure: (i) It has a direct bandgap at the Γ point, unlike the indirect bandgaps of α -TeO₂ and γ -TeO₂; (ii) The bandgap of β -TeO₂ is 2.63 eV, significant smaller than those of α - and γ -TeO₂, correlating with its coloration; (iii) The band edges of β -TeO₂ exhibit high anisotropy, with pronounced dispersion along the Γ –Y and Γ –X directions and localized behavior along the Γ –Z direction, reflecting its layered structure.



Supplementary Fig. 3 | Calculated defect transition levels: a, 3D β - TeO_2 bulk, b, 2D β - TeO_2 monolayer. “ E_v ” and “ E_c ” represent the valence band maximum and conduction band minimum, respectively.

Similar to PbO ,⁸ all intrinsic defects in β - TeO_2 exhibit deep transition levels (Supplementary Fig. 3a). Specifically, the two distinct oxygen vacancies (V_{O1} and V_{O2}) show $(+2/0)$ transitions at 1.69 eV and 1.42 eV below the CBM, respectively, indicating they exist in neutral states when E_F is close to CBM. On the other hand, the calculated $(0/-2)$ transition of Te vacancy (V_{Te}) is at 0.36 eV above the VBM. This deep transition is explained by the insufficient contribution of Te $5s^2$ orbital to the VBM. Notably, the V_{Te} is a negative U system, exhibits a $(+2/-2)$ transition at 0.38 eV above the VBM, so the V_{Te} acts not as an acceptor but rather as a hole trap when the E_F is in the p -type region. The Te interstitial (Te_i) possesses a $(0/+2)$ transition at 0.67 eV below the CBM, while the oxygen interstitial (O_i) shows a $(0/-2)$ transition at 1.50 eV above the VBM, indicating that they are ineffective as donors and acceptors, respectively. The three antisite defects (denoted as Te_{O1} , Te_{O2} , and O_{Te}) can be considered as complexes involving the corresponding vacancies and interstitials, and as such, they also exhibit deep transition levels. Compared to 3D β - TeO_2 , the intrinsic defects in 2D β - TeO_2 essentially shows similar deep transition levels (Supplementary Fig. 3b).

Supplementary Table 1 | Data for band alignment. Experimental electron affinities (χ), ionization potentials (IP), and bandgaps (E_g) of typical n -type TCOs (such as ZnO, In₂O₃, and SnO₂), typical p -type TCOs (such as SnO, NiO, and CuAlO₂) and compounds considered but found challenging to dope as p -type (such as PbO and CsPbCl₃)

Compound	Measured parameters	Derived parameters
ZnO	χ : 4.35 eV; ⁹ E_g : 3.3 eV ⁹	$IP = \chi + E_g = 7.65$ eV
In ₂ O ₃ ^a	IP : 7.10 eV; ¹⁰ E_g : 2.63 eV ¹¹ (3.6 eV ¹¹)	$\chi = IP - E_g = 4.47$ eV (3.5 eV)
SnO ₂	χ : 4.53 eV; ¹² 3.6 eV ¹³	$IP = \chi + E_g = 8.13$ eV
SnO ^a	IP : 5.8 eV; ¹⁴ E_g : 0.7 eV ¹⁴ (2.7 eV ¹⁴)	$\chi = IP - E_g = 5.1$ eV (3.1 eV)
NiO	IP : 5.4 eV; ¹⁵ E_g : 3.7 eV ¹⁵	$\chi = IP - E_g = 1.7$ eV
CuAlO ₂ ^a	IP : 5.24 eV; ¹⁶ E_g : 2.99 eV ¹⁷ (5.33 eV ¹⁷)	$\chi = IP - E_g = 2.25$ eV (1.71 eV)
PbO	IP : 6.2 eV; ⁸ E_g : 2.8 eV ⁸	$\chi = IP - E_g = 3.4$ eV

^aFor indirect bandgap semiconductors, the direct bandgap values are all provided in parentheses; correspondingly, the “ χ ” values derived using the direct bandgaps are also given in parentheses following χ .

Supplementary Table 2 | Atomic orbital energies (eV) relative to the vacuum level.

Element	O	Sn	Pb	Sb	Bi	Te	Po
Outermost p orbital	2p: -9.0	5p: -3.7	6p: -3.5	5p: -4.8	6p: -4.5	5p: -5.9	6p: -5.6
Outermost s orbital	2s: -23.9	5s: -10.5	6s: -12.0	5s: -12.8	6s: -14.4	5s: -15.1	6s: -16.9

Supplementary Table 3 | Calculated electrical parameters. Calculated equilibrium Fermi level ($E_{F,e}$) relative to the VBM, electron density (n_0), and hole density (p_0) as a function of the growth temperature (T_G) for 3D β -TeO₂ bulk and 2D β -TeO₂ monolayer under Te-rich and O-rich conditions. The unit of T_G is K, the unit of $E_{F,e}$ is eV, and the units of n_0 and p_0 are cm⁻³ for 3D β -TeO₂ and cm⁻² for 2D β -TeO₂.

T_G	3D β -TeO ₂						2D β -TeO ₂					
	Te-rich			O-rich			Te-rich			O-rich		
	$E_{F,e}$	n_0	p_0	$E_{F,e}$	n_0	p_0	$E_{F,e}$	n_0	p_0	$E_{F,e}$	n_0	p_0
300	1.37	9.5E-05	5.5E-03	1.25	8.1E-03	6.4E-05	1.71	1.1E-16	1.5E-11	1.38	3.1E-11	5.3E-17
350	1.42	1.1E-05	4.7E-02	1.06	1.3E+01	4.1E-08	1.76	1.6E-17	1.0E-10	1.34	1.5E-10	1.1E-17
400	1.47	2.1E-06	2.4E-01	0.94	1.7E+03	3.1E-10	1.74	3.5E-17	4.7E-11	1.36	6.7E-11	2.5E-17
450	1.50	6.0E-07	8.6E-01	0.83	1.2E+05	4.2E-12	1.72	7.7E-17	2.1E-11	1.41	1.2E-11	1.4E-16
500	1.53	1.8E-07	2.8E+00	0.74	3.9E+06	1.3E-13	1.70	1.3E-16	1.3E-11	1.44	3.0E-12	5.5E-16
550	1.62	6.0E-09	8.6E+01	0.66	6.8E+07	7.6E-15	1.69	2.0E-16	8.3E-12	1.47	1.1E-12	1.5E-15
600	1.71	1.6E-10	3.1E+03	0.60	7.3E+08	7.0E-16	1.68	2.8E-16	6.0E-12	1.49	5.5E-13	3.0E-15
650	1.79	8.0E-12	6.4E+04	0.55	5.5E+09	9.4E-17	1.68	3.7E-16	4.5E-12	1.50	3.4E-13	4.8E-15
700	1.85	6.3E-13	8.2E+05	0.50	3.1E+10	1.7E-17	1.67	4.6E-16	3.6E-12	1.51	2.4E-13	6.9E-15

Computational methods

First-principles calculations were conducted in the framework of density functional theory using the projector-augmented wave method implemented within the Vienna Ab initio Simulation Package (VASP 6.4.3 code).¹⁸ A plane-wave cutoff energy of 500 eV was employed. For TeO₂ polymorphs and their competing phases (Te, Te₄O₉, Te₂O₅, TeO₃, and O₂), Γ -centered k -meshes with a k -point spacing of 0.2 \AA^{-1} were utilized to sample the Brillouin zones. The crystal or molecular structures were fully relaxed using the PBE functional¹⁹ until the forces on each atom were less than 0.01 eV/ \AA . The PBE¹⁹ functional, known for significantly underestimating the bandgaps for oxides, slightly underestimates those of TeO₂ polymorphs. Specifically, the PBE-calculated bandgaps for α - and γ -TeO₂ are 2.79 eV and 3.06 eV, respectively, which are relatively close to their experimental values (3.48 eV²⁰ and 3.41 eV,²¹ respectively). Conversely, the HSE^{22,23} hybrid functional with a standard mixing parameter of 0.25 (HSE^{0.25}), overestimates these bandgaps. The HSE^{0.25}-calculated bandgaps for α - and γ -TeO₂ are 3.89 eV and 4.21 eV, notably higher than experimental values. Similarly, for β -TeO₂, which is yellow, the HSE^{0.25} predicts a bandgap approximately 3.3 eV, inconsistent with its observed color. To gain more accurate bandgaps for TeO₂ polymorphs, the HSE functional with a reduced mixing parameter of 0.10 (HSE^{0.10}) was examined. The HSE^{0.10}-calculated bandgaps for α - and γ -TeO₂ are 3.21 eV and 3.51 eV, closely aligning with experimental values, while the HSE^{0.10} bandgap for β -TeO₂ is 2.63 eV, consistent with its yellow appearance.^{3,4} Consequently, the mixing parameter was optimized to 0.10 to roughly reproduce the experimental bandgaps and this value is applied for electronic structure and total energy calculations.

In the case of the 2D β -TeO₂ monolayer and multilayers, the slab models were fully relaxed with the c lattice parameter constrained. For the β -TeO₂ monolayer, the c lattice parameter of the slab model was constrained to 12.255 \AA , corresponding to the relaxed c lattice parameter of bulk β -TeO₂. The thickness of the included vacuum layer (approximately 8.2 \AA) has been confirmed to provide reasonably convergent results (cf. calculated bandgaps of 2.667 eV, 2.660 eV and 2.674 eV for vacuum thicknesses of 8.2 \AA , 13.9 \AA and 20.9 \AA , respectively).

The CBMs and VBMs (with respect to the vacuum level) of the TeO₂ polymorphs were determined by the methodology described in Ref. 24. (001) surface models with vacuum thickness of 15 \AA were used. For bulk α -, β -, and γ -TeO₂ polymorphs, the slab thickness were 15–27 \AA . The ionization potential (IP) and electron affinity (χ) were calculated using a bulk-based definition via electrostatic alignment between the surface and the bulk as

$$\begin{aligned}\varepsilon_{\text{IP}} &= \Delta\varepsilon_{\text{vac-ref}} - \Delta\varepsilon_{\text{VBM-ref}} \\ \varepsilon_{\chi} &= \Delta\varepsilon_{\text{vac-ref}} - \Delta\varepsilon_{\text{CBM-ref}}\end{aligned}\tag{1}$$

where $\Delta\varepsilon_{\text{vac-ref}}$ is the energy difference between the electrostatic potential in the vacuum region, namely the vacuum level, and the reference level in a bulk-like region of a surface supercell. $\Delta\varepsilon_{\text{VBM-ref}}$ and $\Delta\varepsilon_{\text{CBM-ref}}$ are the energy differences between the VBM and the reference level and between CBM and the reference level, respectively. The VBMs and CBMs are aligned using the negatives of the IP and the χ , respectively.

For β -TeO₂ bulk and monolayer, defect calculations were carried out using $2\times 2\times 1$ supercells with an effective size (the cube root of the supercell volume) of approximately 11.6 \AA (containing 96 and 48 atoms, respectively) and a single Γ k -point. Using the oxygen vacancies

in the β -TeO₂ monolayer as an example, a convergence test indicates that the errors in defect formation energies between the employed supercell and a larger supercell (a $2 \times 2 \times 1$ supercell with $c = 18$ Å and an effective size of 17.6 Å) are within 0.1 eV (e.g., for V_{O2}²⁺ in the β -TeO₂ monolayer, the ΔH values at $E_F = E_V$ are -1.85 eV and -1.80 eV for supercell sizes of 11.6 Å and 17.6 Å, respectively), which is considered sufficient convergence for the purpose of this work. The lattice parameters of the defective supercell were constrained, while the atomic positions were relaxed using the PBE functional until the forces on each atom were less than 0.03 eV/Å. The total energies were calculated using the HSE^{0.10}.

For a defect (α) in a charge state q , the formation energy $\Delta H_{\alpha,q}$ was calculated by the equation²⁵

$$\Delta H_{\alpha,q} = E_{\alpha,q} - E_h + q(E_V + E_F) + \sum n_i \mu_i, \quad (2)$$

where $E_{\alpha,q}$ is the total energy of the supercell with the defect (α) in the charge q obtained by the self-consistent potential correction (SCPC) method²⁶ implemented in the VASP 6.4.3 package and E_h is that of the perfect host supercell. E_F is the Fermi level referred to VBM, E_V . n_i indicates the number of i atom added ($n_i < 0$) or removed ($n_i > 0$) when a defect is formed, and μ_i is the chemical potential of the i atom which can be expressed with respect to that of an element phase (μ_i^{el}) by $\mu_i = \mu_i^{\text{el}} + \Delta\mu_i$.

The charge transition level $\varepsilon(q/q')$ was calculated by the equation

$$\varepsilon(q/q') = \frac{\Delta H_{\alpha,q'} - \Delta H_{\alpha,q}}{q - q'}, \quad (3)$$

where $\Delta H_{\alpha,q}$ and $\Delta H_{\alpha,q'}$ are the formation energies of a defect α at the charge states q and q' , respectively.

The defect density was calculated by the statistic equation

$$c_{\alpha,q}(E_F, \mu, T_G) = N_{\alpha,q} \exp\left[\frac{-c_{\alpha,q}(E_F, \mu)}{k_B T_G}\right], \quad (4)$$

where $N_{\alpha,q}$ is density of possible sites for defects, k_B is the Boltzmann constant, and T_G is the growth temperature at which defects are formed and assumed to be frozen at room temperature (300 K). The equilibrium E_F ($E_{F,e}$) was determined by solving the following semiconductor statistic equations self-consistently to satisfy the charge neutrality condition:²⁷

$$\sum_j \sum_k q_k c_{\alpha_j, q_k} - n_0 + p_0 = 0, \quad (5)$$

$$\sum_j \sum_k q_k c_{\alpha_j, q_k} - n_0 + p_0 = 0$$

$$n_0 = 2 \left(\frac{2\pi m_e^* k_B T}{h^2} \right)^{3/2} \exp\left[\frac{-(E_c - E_F)}{k_B T}\right], \quad (6)$$

$$p_0 = 2 \left(\frac{2\pi m_h^* k_B T}{h^2} \right)^{3/2} \exp \left[\frac{-(E_F - E_v)}{k_B T} \right], \quad (7)$$

where E_c and E_v are the CBM and VBM, respectively; m_e^* and m_h^* are effective masses of electrons and holes, respectively; h is the Planck constant; T is the temperature for measuring electrical properties.

Supplementary references

1. Leciejewicz, J. The crystal structure of tellurium dioxide. A redetermination by neutron diffraction. *Zeitschrift für Krist.* **116**, 345–353 (1961).
2. Worlton, T. G. & Beyerlein, R. A. Structure and order parameters in the pressure-induced continuous transition in TeO₂. *Phys. Rev. B* **12**, 1899–1907 (1975).
3. Ito, T. & Sawada, H. The Crystal Structure of Tellurite (TeO₂). *Zeitschrift für Krist. - Cryst. Mater.* **102**, 13–25 (1940).
4. Beyer, H. Verfeinerung der Kristallstruktur von Tellurit, dem rhombischen TeO₂. *Zeitschrift für Krist.* **124**, 228–237 (1967).
5. Zavabeti, A. *et al.* High-mobility p-type semiconducting two-dimensional β -TeO₂. *Nat. Electron.* **4**, 277–283 (2021).
6. Guo, S. *et al.* Ultrathin tellurium dioxide: emerging direct bandgap semiconductor with high-mobility transport anisotropy. *Nanoscale* **10**, 8397–8403 (2018).
7. Peng, K. *et al.* Observation of metallic TeO₂ thin film with rutile structure on FeTe surface. *J. Mater. Sci.* **57**, 10225–10232 (2022).
8. Liao, M. *et al.* Difficulty of carrier generation in orthorhombic PbO. *J. Appl. Phys.* **119**, 165701 (2016).
9. Aranovich, J. A., Golmayo, D., Fahrenbruch, A. L. & Bube, R. H. Photovoltaic properties of ZnO/CdTe heterojunctions prepared by spray pyrolysis. *J. Appl. Phys.* **51**, 4260–4268 (1980).
10. Hohmann, M. V. *et al.* Orientation dependent ionization potential of In₂O₃: a natural source for inhomogeneous barrier formation at electrode interfaces in organic electronics. *J. Phys. Condens. Matter* **23**, 334203 (2011).
11. Köstlin, H., Jost, R. & Lems, W. Optical and electrical properties of doped In₂O₃ films. *Phys. Status Solidi* **29**, 87–93 (1975).
12. Islam, M. N. & Hakim, M. O. Electron affinity and work function of polycrystalline SnO₂ thin film. *J. Mater. Sci. Lett.* **5**, 63–65 (1986).
13. Summitt, R., Marley, J. A. & Borrelli, N. F. The ultraviolet absorption edge of stannic oxide (SnO₂). *J. Phys. Chem. Solids* **25**, 1465–1469 (1964).
14. Nomura, K., Kamiya, T. & Hosono, H. Ambipolar Oxide Thin-Film Transistor. *Adv. Mater.* **23**, 3431–3434 (2011).
15. Fu, G. *et al.* Tuning the Electronic Structure of NiO via Li Doping for the Fast Oxygen Evolution Reaction. *Chem. Mater.* **31**, 419–428 (2019).
16. Brahimi, R., Bellal, B., Bessekhoud, Y., Bouguelia, A. & Trari, M. Physical properties of CuAlO₂ single crystal. *J. Cryst. Growth* **310**, 4325–4329 (2008).
17. Pellicer-Porres, J. *et al.* On the band gap of CuAlO₂ delafossite. *Appl. Phys. Lett.* **88**, 2–5 (2006).
18. Kresse, G. & Furthmüller, J. Efficient iterative schemes for ab initio total-energy calculations using a plane-wave basis set. *Phys. Rev. B* **54**, 11169–11186 (1996).
19. Perdew, J. P., Burke, K. & Ernzerhof, M. Generalized Gradient Approximation Made Simple. *Phys. Rev. Lett.* **77**, 3865–3868 (1996).
20. Siciliano, T. *et al.* Transition from n- to p-type electrical conductivity induced by ethanol adsorption on α -tellurium dioxide nanowires. *Sensors Actuators B Chem.* **138**, 207–213 (2009).
21. Dewan, N., Sreenivas, K. & Gupta, V. Properties of crystalline γ -TeO₂ thin film. *J. Cryst.*

- Growth* **305**, 237–241 (2007).
22. Heyd, J., Scuseria, G. E. & Ernzerhof, M. Hybrid functionals based on a screened Coulomb potential. *J. Chem. Phys.* **118**, 8207–8215 (2003).
 23. Heyd, J., Scuseria, G. E. & Ernzerhof, M. Erratum: “Hybrid functionals based on a screened Coulomb potential” [J. Chem. Phys. 118, 8207 (2003)]. *J. Chem. Phys.* **124**, 219906 (2006).
 24. Hinuma, Y., Gr, A., Kresse, G. & Oba, F. Band alignment of semiconductors from density-functional theory and many-body perturbation theory. **155405**, 1–16 (2014).
 25. Van de Walle, C. G. First-principles calculations for defects and impurities: Applications to III-nitrides. *J. Appl. Phys.* **95**, 3851–3879 (2004).
 26. Chagas da Silva, M. *et al.* Self-Consistent Potential Correction for Charged Periodic Systems. *Phys. Rev. Lett.* **126**, 076401 (2021).
 27. Yang, J.-H. *et al.* Tuning the Fermi level beyond the equilibrium doping limit through quenching: The case of CdTe. *Phys. Rev. B* **90**, 245202 (2014).